



OPEN

# Enhanced Selectivity Electronic Nose Systems for Agricultural Ammonia Gas Detection via a co-designed $\text{WO}_3$ -ZnO Sensor Array and Convolutional Neural Networks

Mengying Du<sup>1,5</sup>, Mukhtar Iderawumi Abdulraheem<sup>1,2,5</sup>✉, Lulu Xu<sup>1</sup>, Yiheng Zang<sup>1</sup>, Yinghang Song<sup>1</sup>, Maryam Abbasi Tarighat<sup>3</sup>✉, Vijaya Raghavan<sup>4</sup> & Jiandong Hu<sup>1</sup>✉

Electronic noses (e-noses) offer a practical solution for real-time monitoring of ammonia ( $\text{NH}_3$ ) in agricultural environments, where  $\text{NH}_3$  often coexists with interfering gases such as  $\text{CO}_2$ ,  $\text{CH}_4$ , and  $\text{H}_2\text{S}$ . However, semiconductor-based gas sensors commonly used in e-nose systems suffer from inherent cross-sensitivity, which reduces measurement accuracy. This study investigates the cross-sensitivity of  $\text{NH}_3$  detection and introduces a mitigation strategy through convolutional neural networks (CNNs) for sensor data fusion. Experimental results show that  $\text{WO}_3$ -based sensors exhibit strong  $\text{NH}_3$  selectivity, with response ratios of 7.3:1 against  $\text{CH}_4$  and 17.8:1 against  $\text{H}_2\text{S}$ . Density functional theory (DFT) analysis confirmed that the  $\text{WO}_3$  sensor exhibited strongest  $\text{NH}_3$  binding energy ( $-1.45$  eV), compared to  $\text{SnO}_2$  ( $-1.10$  eV), explaining the observed selectivity. Measurement uncertainties ( $\pm 8\%$ ) were quantified under varying humidity (30–90% RH) and temperature (10–40 °C) using a weighted least squares error propagation model. A quasi-2D sensor array improved  $\text{NH}_3$  classification accuracy to 96.4% (7.2% increase) while reducing concentration errors by 50.8%, as validated by linear discriminant analysis. Long-term stability tests demonstrated that  $\text{SnO}_2$  sensors maintained a low baseline drift of 0.18%/day over 180 days, outperforming  $\text{CH}_4$  (0.31%/day) and  $\text{ZnO}$  (0.42%/day) sensors. Furthermore, the CNN model, trained on multi-sensor time-series data, achieved 91.7% accuracy in mixed-gas environments by capturing non-linear response patterns, ensuring reliable  $\text{NH}_3$  quantification despite interferences. These findings highlight the promise of CNN-enhanced e-nose systems for precise  $\text{NH}_3$  monitoring in complex agricultural settings, addressing key challenges of cross-sensitivity and environmental stability.

**Keywords** Ammonia gas sensor, Electronic nose (E-nose), Metal-oxide semiconductor, Convolutional neural network (CNN), Sensor data fusion, Agricultural emission monitoring

Ammonia ( $\text{NH}_3$ ) is a critical atmospheric pollutant with significant environmental and health implications<sup>1,2</sup>. In agricultural settings, particularly in livestock farming and fertilized croplands, ammonia emissions are a major concern. High concentrations of ammonia can lead to soil acidification, water eutrophication, and the formation of fine particulate matter ( $\text{PM}_{2.5}$ ) in the atmosphere, posing risks to both ecosystem balance and human health<sup>1,3</sup>. Therefore, accurate and continuous monitoring of ammonia concentrations in agricultural environments

<sup>1</sup>Henan International Joint Laboratory of Laser Technology in Agriculture Sciences, College of Mechanical and Electrical Engineering, Henan Agricultural University, Zhengzhou 450002, China. <sup>2</sup>Department of Agricultural Science Education, Oyo State College of Education, Lanlate, Lanlate 202001, Nigeria. <sup>3</sup>Department of Nano and Bionano Science and Technology, Persian Gulf University, Bushehr 75169, Iran. <sup>4</sup>Department of Bioresource Engineering, Faculty of Agriculture and Environmental Studies, McGill University, Sainte-Anne-de-Bellevue, QC H9X 3V9, Canada. <sup>5</sup>Mengying Du and Mukhtar Iderawumi Abdulraheem contributed equally to this work. ✉email: m.iderawumi@gmail.com; abdulraheem@stu.henau.edu.cn; matarighat@pgu.ac.ir; jdhu@henau.edu.cn

is crucial for effective environmental management and optimizing agricultural practices<sup>4,5</sup>. Electronic noses (E-noses) have emerged as a promising solution for real-time gas monitoring leveraging arrays of semi-selective chemical sensors combined with pattern recognition<sup>6,7</sup>. However, a fundamental challenge persists: cross-sensitivity, where sensors respond to multiple gases simultaneously, leading to inaccurate identification and quantification of the target analyte in complex mixtures like those found in agricultural environments ( $\text{NH}_3$ ,  $\text{CO}_2$ ,  $\text{CH}_4$ ,  $\text{H}_2\text{S}$ )<sup>8,9</sup>.

The evolution of electronic noses is increasingly geared towards integration with the Internet of Things (IoT) for real-time, distributed environmental monitoring<sup>10</sup>. These systems demand not only high sensor performance but also reliability, low power consumption, and intelligent data processing capabilities. Our work directly contributes to this paradigm by developing a robust e-nose system that combines optimized sensing materials with advanced machine learning, addressing the critical need for accurate and autonomous gas monitoring in agricultural IoT applications. The application of deep learning, particularly convolutional neural networks (CNNs), to e-nose data has gained considerable momentum for addressing cross-sensitivity. Recent literature demonstrates both the potential and limitations of existing approaches. Yang and Wang<sup>11</sup> proposed a CNN model with an attentional mechanism for discriminating hazardous gas mixtures. Their system achieved high accuracy in laboratory settings but was primarily tested on binary and ternary mixtures, leaving its performance in more complex, multi-component agricultural atmospheres unverified. Furthermore, the study did not integrate material-level selectivity analysis with the data fusion mode. Moshayedi and Sohail Khan<sup>12</sup> conducted a comprehensive review of e-nose advancements for ammonia detection, highlighting the promise of CNNs but also noting a significant gap in long-term stability studies and the lack of synergy between sensor material optimization and algorithmic approaches<sup>13–15</sup>. Most studies focused solely on the algorithm without co-designing the sensor array for complementary responses. Recent study by Mor et al.<sup>16</sup> explored the gas sensor market trends, emphasizing the need for solutions that are robust to environmental variables like humidity and temperature<sup>17</sup>. Their work indicated that while CNNs are effective, their performance degrades significantly without explicit architectural considerations for temporal drift and environmental interference, a common oversight in many proposed models.

Another study by Liu et al.<sup>8</sup> developed an optical dual gas sensor for resolving cross-sensitivity between oxygen and ammonia using fluorescence quenching. While effective, this approach relies on specialized optical equipment, which increases the system's cost and complexity compared to semiconductor-based e-noses, limiting its practicality for widespread agricultural deployment. Recent advancements in nanomaterial engineering have demonstrated promising pathways to improving gas sensor sensitivity and stability. For instance, novel nanostructures and surface functionalization techniques have been explored to enhance the response to various target gases<sup>18–20</sup>. Despite these material-level improvements, achieving high selectivity in complex gas mixtures remains a fundamental challenge. Cross-sensitivity to interfering species continues to limit the accuracy of metal-oxide-based sensors in real-world environments<sup>21</sup>. This work addresses this gap by proposing a synergistic approach that leverages both material selection ( $\text{WO}_3$ ) and a co-designed sensor array and CNN algorithm to effectively decouple the target  $\text{NH}_3$  signal from interferents like  $\text{CH}_4$ ,  $\text{H}_2\text{S}$ , and  $\text{CO}_2$ . A critical analysis of the literature reveals three predominant gaps:

1. *Algorithm-Material Disconnect*: A siloed approach where advanced algorithms are applied to standard, off-the-shelf sensor arrays without optimizing the array's material composition for complementary cross-sensitivity patterns
2. *Limited Environmental Robustness*: Models are often trained and validated under ideal conditions, with insufficient focus on performance under varying humidity, temperature, and long-term drift typical of agricultural settings.
3. *Lack of Explainability*: Many CNN models operate as "black boxes," lacking interpretation that links the model's decisions to the underlying physicochemical principles of gas-sensor interactions.

This paper presents a holistic strategy to overcome the limitation of cross-sensitivity in e-nose systems for agricultural ammonia monitoring. This paper presents a holistic strategy to overcome the limitation of cross-sensitivity in e-nose systems for agricultural ammonia monitoring. The major contributions of this work are as follows:

- *A Co-Designed Sensor Array and Algorithm Framework*: We introduce a quasi-2D complementary sensor array that strategically combines  $\text{WO}_3$  and  $\text{ZnO}$  sensors based on their orthogonal response characteristics. This array is not a standard off-the-shelf selection but is explicitly designed to provide maximally informative input features for a subsequent convolutional neural network (CNN), enabling effective cross-sensitivity decoupling.
- *A Physicistically-Informed CNN Architecture*: We develop a custom 1D-CNN architecture that is tailored to leverage temporal response patterns from the sensor array. The design is informed by Density Functional Theory (DFT) calculations of adsorption energies, creating a more interpretable link between the underlying material properties and the model's feature extraction process.
- *Comprehensive Validation Under Realistic Conditions*: We provide an extensive evaluation of the system's performance not only in controlled mixed-gas environments but also under realistic environmental stressors, including wide-ranging humidity, temperature variations, and a long-term stability assessment over 180 days—metrics often absent in related literature.
- *A Complete Workflow from Mechanism to Application*: This work bridges a critical gap by integrating material-level selectivity analysis, sensor array design, and advanced data fusion into a single, validated workflow, demonstrating a clear pathway from fundamental principles to a functional, field-ready sensing system.

## Methods and instrumentation

The successful development of an electronic nose for ammonia detection relies on a well-designed measurement system that can accurately generate controlled gas mixtures, expose the sensor array to these mixtures in a reproducible manner, and acquire the resulting sensor data for analysis. This section details the design of the measurement system used in this study, covering the fundamental principles of the semiconductor sensors employed and the comprehensive experimental setup.

### The principle of ammonia gas measurement using semiconductor sensors

Semiconductor gas sensors, specifically n-type Metal Oxide Semiconductor (MOS) sensors, form the core of the e-nose system. The fundamental working principle is based on measurement changes in electrical resistance upon interaction with target gas molecules (Fig. 1). The sensor array comprised multiple metal oxide sensors, including the Grove Multi Gas Sensor V2 series (GM-102B, GM-302B, GM-502B, GM-702B), MQ135, MQ137, and TGS2602, fabricated via MEMS technology. A dedicated BME688 sensor provided simultaneous environmental monitoring of temperature and humidity. Figure 1c,d illustrates the integrated sensor unit with its corresponding circuit diagram and physical device. For n-type metal oxide semiconductors ( $\text{SnO}_2$ ,  $\text{ZnO}$ ,  $\text{WO}_3$ ), the sensing mechanism involves the adsorption of oxygen species ( $\text{O}_2$ ,  $\text{O}^-$ ,  $\text{O}^{2-}$ ) on the semiconductor surface at elevated operating temperatures (typically 150–400 °C)<sup>22–24</sup>. These adsorbed oxygen species capture electrons from the conduction band, forming a depletion layer and increasing the sensor's resistance in clean air. When a reducing gas such as ammonia ( $\text{NH}_3$ ) is introduced, it reacts with the pre-adsorbed oxygen ions through surface reactions, releasing the trapped electrons back into the conduction band. This process decreases the depletion layer width and reduces the sensor's electrical resistance proportionally to the gas concentration<sup>25</sup>.

Figure 1a illustrates the underlying  $\text{NH}_3$  detection mechanism for MQ137, which employs  $\text{SnO}_2$  as its sensitive material. When  $\text{NH}_3$  interacts with the n-type MOS surface, electrons are donated to the conduction band, reducing the depletion layer width and increasing conductivity (resistance decrease). The sensor response was quantified by the voltage drop across a load resistor ( $R_L$ ) in series with the sensor under a constant bias voltage ( $V_{H-} = 5$  V). The baseline resistance ( $R_0$ ) was established for each sensor through a 30-min stabilization period in clean dry air (20%  $\text{O}_2$ , 80%  $\text{N}_2$ ) prior to each measurement sequence. All sensors were operated in a temperature-stabilized laboratory environment ( $23 \pm 1$  °C) with electromagnetic interference shielding to minimize external noise. The sensor's cross-sensitivity to other amines (e.g., dimethylamine) follows a similar electron donation mechanism, albeit with varying charge transfer efficiencies (Q1 = 1E, Q2 = 2E, Q3 = 3E). The experimental setup, as illustrated in Fig. 1b, is designed to facilitate controlled and reproducible experiments for studying the response of the e-nose system to ammonia and other interfering gases. The setup is composed of three main subsystems: a gas generation and delivery system, a measurement chamber, and a data acquisition and control system.

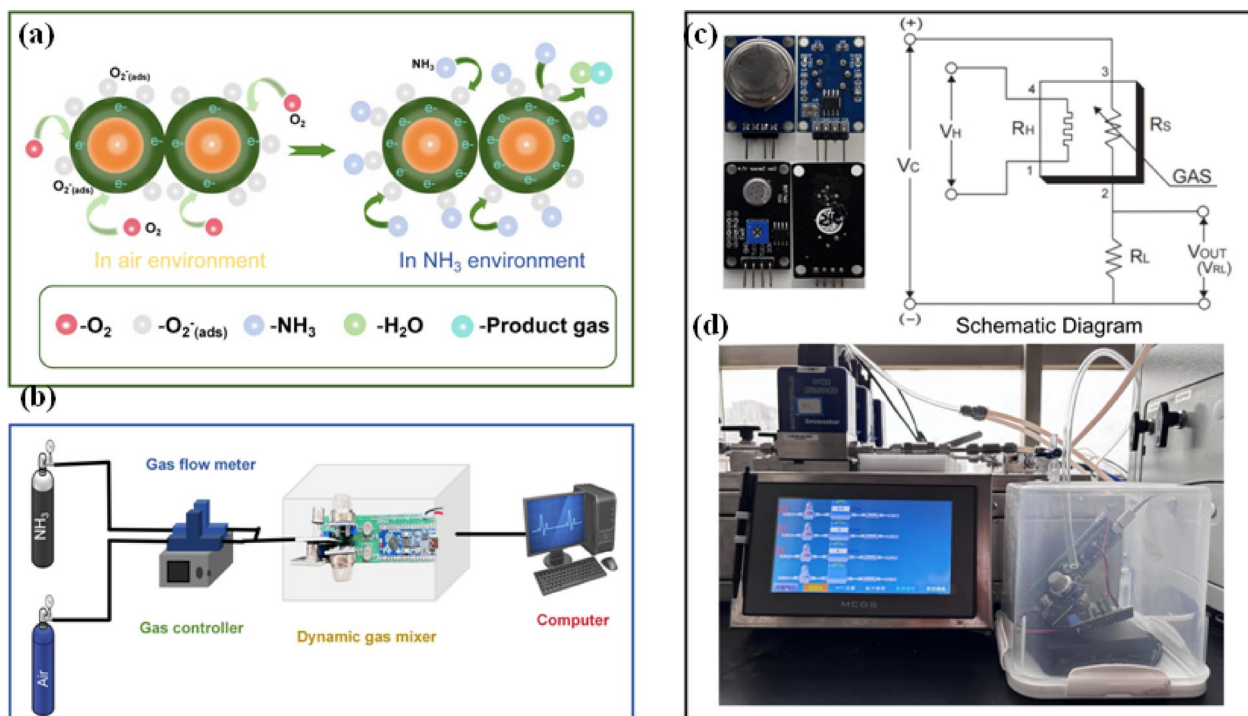


**Fig. 1.** Integrated MOXgas sensor system and experimental setup, (a) Microscopic gas-sensing mechanism of the MQ-137 ammonia ( $\text{NH}_3$ ) sensor (b) Gas testing system configuration. (c) Sensor unit with corresponding circuit diagram (d) Optical photograph of physical device.

## Experimental set-up and gas generation system

A custom experimental apparatus was designed to facilitate controlled and reproducible testing of the sensor array under conditions simulating agricultural environments. The system, illustrated in Fig. 1b, comprises three integrated subsystems: a precision gas generation and delivery system, a thermally and environmentally controlled measurement chamber, and a centralized data acquisition unit. The core of the gas generation system was a custom mixing station equipped with four mass flow controllers (MFCs, Alicat Scientific,  $\pm 1\%$  full-scale accuracy). The selected concentration ranges were carefully chosen to reflect realistic agricultural conditions based on literature reports<sup>26,27</sup>.  $\text{CH}_4$  concentrations in animal housing generally vary between 50–400 ppm, while  $\text{CO}_2$ , primarily from animal respiration, commonly falls in the 1000–4000 ppm range but can reach higher levels<sup>28</sup>. The  $\text{H}_2\text{S}$  range (1–50 ppm) covers both background levels and peak concentrations near manure storage, where it can pose health risks above 10–20 ppm<sup>8</sup>. These ranges ensure the system is tested under conditions relevant to its intended agricultural deployment, covering both typical operating scenarios and challenging interference conditions. The multi-component gas flow was modeled using a Navier–Stokes–Dusty Gas Model to ensure homogeneity<sup>29</sup>:

$$\frac{\partial C_i}{\partial t} = D_i \nabla^2 C_i - v \cdot \Delta C_i + R_i \quad (1)$$

where  $D_i = 0.205 \text{ cm}^2/\text{s}$  and ( $\pm 1\%$  accuracy). The MFCs were calibrated to deliver precise, dynamic mixtures of target and interference gases in a dry air balance (20%  $\text{O}_2$ , 80%  $\text{N}_2$ ). The selection of these ranges was justified in Section “**Sensor response quantification and experimental protocol**”. Gas concentrations adhered to ISO 6143 standards, with certified calibration gases (NPL-traceable) used for periodic system validation. The sensor array was housed within a 5L stainless steel test chamber. A PID-controlled heater ( $25\text{--}400^\circ\text{C} \pm 0.5^\circ\text{C}$ ) and a humidity generator (30–90% RH  $\pm 2\%$ ) were integrated into the chamber to precisely simulate the temperature and humidity fluctuations typical of farmland conditions<sup>30,31</sup>. The sensor array consisted of a strategically selected combination of commercial metal-oxide (MOX) sensors and a dedicated environmental sensor. Table 1 provides a complete summary of the sensor models, their primary target gases, and the operating parameters tested.

The data acquisition and control system was built around an Arduino Mega 2560 microcontroller, which managed the MFCs, chamber temperature, and humidity setpoints. Sensor analog voltage outputs were recorded at a sampling frequency of 1 Hz using a 16-bit ADC (NI-9215, National Instruments) to capture the full dynamic response. The entire setup was housed in a temperature-stabilized laboratory ( $23 \pm 1^\circ\text{C}$ ) with electromagnetic interference shielding to minimize external noise.

## Sensor response quantification and experimental protocol

*Sensor response calculation:* The sensor response to target gases was quantified using the relative resistance change, defined as:

$$\text{Response (\%)} = [(\text{Ro} - \text{Rg})/\text{Ro}] \times 100 \quad (2)$$

where  $\text{R}_0$  is the stable baseline resistance in dry, clean synthetic air, and  $\text{R}_g$  is the steady-state resistance upon exposure to the target gas. The steady-state value was determined as the average resistance over the final 10 s of a 60-s gas exposure period, once the signal had stabilized (change  $< 1\%/\text{s}$ ). For sensors where resistance decreased upon gas exposure (n-type behavior), this formulation yields positive response values.

*Concentration range justification:* The gas concentration ranges were selected based on two primary considerations: agricultural relevance and sensor operational characteristics. The  $\text{NH}_3$  range (1–100 ppm) covers typical concentrations in livestock facilities (5–50 ppm) while extending to higher levels encountered in poorly ventilated areas<sup>32,33</sup>.  $\text{CH}_4$  concentrations (10–500 ppm) represent levels found in animal housing, while  $\text{CO}_2$  (100–5000 ppm) spans background to peak respiration levels<sup>28,34</sup>. The  $\text{H}_2\text{S}$  range (1–50 ppm) addresses both background levels and hazardous concentrations near manure storage<sup>35</sup>. These ranges ensure the system is tested under conditions spanning normal operation to challenging interference scenarios.

*Operating temperature optimization:* Sensor operating temperatures were optimized through preliminary characterization experiments measuring response to 50 ppm  $\text{NH}_3$  across temperature ranges ( $150\text{--}400^\circ\text{C}$ ).

| Sensor type   | Model/configuration          | Target gases                                       | Operating temperature range tested ( $^\circ\text{C}$ ) | Manufacturer/configuration |
|---------------|------------------------------|--|---|----------------------------|
| Metal oxide   | Grove Multi-Gas V2 (GM-102B) | $\text{CO}, \text{CO}_2, \text{NH}_3, \text{CH}_4$ | 150–350   | Seeed Studio               |
| Metal oxide   | Grove Multi-Gas V2 (GM-302B) | $\text{CO}, \text{Alcohols}, \text{NH}_3$          | 150–350   | Seeed Studio               |
| Metal oxide   | Grove Multi-Gas V2 (GM-502B) | $\text{H}_2, \text{CH}_4, \text{CO}$               | 150–350   | Seeed Studio               |
| Metal oxide   | Grove Multi-Gas V2 (GM-702B) | $\text{H}_2\text{S}, \text{NH}_3, \text{CO}$       | 150–350   | Seeed Studio               |
| Metal oxide   | MQ135                        | $\text{NH}_3, \text{NO}_x, \text{CO}_2$            | 150–300   | Hanwei Electronics         |
| Metal oxide   | MQ137                        | $\text{NH}_3$                                      | 150–300   | Hanwei Electronics         |
| Metal oxide   | TGS2602                      | $\text{NH}_3, \text{H}_2\text{S}$                  | 150–300   | Figaro Engineering         |
| Environmental | BME688                       | Temperature, Humidity                              | –40 to +85  | Bosch Sensortec            |

**Table 1.** Sensor specifications and experimental parameters used in the study. Note: All metal oxide sensors were operated within their manufacturer-specified temperature ranges, with specific operating temperatures optimized for  $\text{NH}_3$  detection.

Each sensor material exhibited a temperature-dependent response profile:  $\text{WO}_3$  showed optimal response at  $250 \pm 10^\circ\text{C}$ ,  $\text{SnO}_2$  at  $300 \pm 10^\circ\text{C}$ , and  $\text{ZnO}$  at  $200 \pm 10^\circ\text{C}$ . These temperatures represent the compromise between maximizing sensitivity to  $\text{NH}_3$  and minimizing cross-sensitivity to interfering gases, as determined through signal-to-interference ratio analysis.

**Measurement protocol:** All experiments followed a standardized sequence: (1) 30-min baseline stabilization in synthetic air at the specified operating temperature; (2) 60-s exposure to target gas mixture; (3) 120-s recovery in synthetic air. Each concentration was tested in triplicate, with randomized presentation order to minimize sequence effects. Environmental conditions (temperature:  $23 \pm 1^\circ\text{C}$ , humidity:  $50 \pm 5\%$  RH unless varied intentionally) were continuously monitored and recorded.

### Long-term stability testing protocol

Long-term stability testing was conducted over a continuous 180-day period to evaluate sensor degradation under simulated agricultural conditions. Sensors were operated in a controlled environmental chamber that applied cyclic variations representative of typical farmland conditions: temperature cycles between  $15^\circ\text{C}$  (night) and  $35^\circ\text{C}$  (day), and humidity cycles between 40% RH (day) and 80% RH (night). Baseline resistance measurements were recorded automatically every 6 h throughout the entire testing period. The sensors were periodically exposed to calibration gas mixtures (50 ppm  $\text{NH}_3$  in dry air) every 14 days to track sensitivity changes. This protocol provided a comprehensive dataset for assessing both gradual drift and cyclic environmental effects on sensor performance.

### DFT computational methods

Density Functional Theory (DFT) calculations were performed to compute the adsorption energies of gas molecules ( $\text{NH}_3$ ,  $\text{CH}_4$ ,  $\text{H}_2\text{S}$ ) on the metal oxide surfaces ( $\text{WO}_3$ ,  $\text{SnO}_2$ ,  $\text{ZnO}$ ) to provide a theoretical basis for the observed sensor selectivity<sup>18</sup>. All calculations were conducted using the Vienna Ab initio Simulation Package (VASP)<sup>36,37</sup>. The electron interactions were described with the Perdew-Burke-Ernzerhof (PBE) generalized gradient approximation functional<sup>38</sup>, and Grimme's DFT-D3 dispersion correction was included to account for van der Waals forces<sup>39</sup>. The projector augmented-wave (PAW) method was used for the core-valence electron interaction<sup>40</sup>. A plane-wave basis set with a cutoff energy of 520 eV was employed. The Brillouin zone was sampled with a  $3 \times 3 \times 1$  Monkhorst-Pack k-point mesh for surface calculations<sup>41</sup>. Geometry optimizations were performed until the forces on all atoms were below  $0.02 \text{ eV}/\text{\AA}$ , with an energy convergence criterion of  $10^{-5} \text{ eV}$ . The adsorption energy ( $E_{\text{ads}}$ ) was calculated using the standard formula:

$$E_{\text{ads}} = E(\text{surface} + \text{mol}) - E(\text{surface}) - E(\text{mol}) \quad (3)$$

where  $E(\text{surface} + \text{mol})$  is the total energy of the optimized surface with the adsorbed molecule,  $E(\text{surface})$  is the energy of the clean surface, and  $E(\text{mol})$  is the energy of the isolated gas molecule in the gas phase.

### Power requirements and drift characteristics

For practical field deployment, the e-nose system's power consumption and inherent drift were characterized. The dominant power demand comes from micro-heaters maintaining MOX sensors at  $150\text{--}350^\circ\text{C}$  operating temperatures, consuming 25–35 mA at 5 V per sensor (125–175 mW each). The 6-sensor array peaks at  $\sim 1.0 \text{ W}$  during heating phases. A pulsed heating strategy during 60-s measurement cycles reduces average sensor array consumption to 350–450 mW. The complete system, including microcontroller and data acquisition, requires 500–650 mW during active operation, enabling battery or solar-powered deployment. Inherent sensor drift includes baseline drift (resistance shift in clean air) and sensitivity drift (response magnitude change), primarily from material morphological changes.  $\text{WO}_3$  demonstrated superior stability with the lowest baseline drift (0.18%/day) and minimal sensitivity variation (<8% over 180 days). The system incorporates automatic baseline correction and requires recalibration every 3–4 months, aligning with agricultural maintenance schedules to ensure sustained field accuracy.

### Mathematics modeling

Accurate quantification of ammonia in complex gas mixtures using an electronic nose necessitates robust mathematical modeling to interpret the multi-sensor responses and mitigate the effects of cross-sensitivity<sup>42</sup>. This section delves into the mathematical framework for sensor response, the proposed convolutional neural network (CNN) architecture for data fusion, and the methodology for calculating ammonia concentration from the fused data.

### Mathematical model for sensor response and cross-sensitivity

To accurately model the behavior of an electronic nose system, it is essential to develop mathematical representations of individual sensor responses and their cross sensitivity to various gases<sup>10</sup>. The response of a semiconductor gas sensor is typically characterized by a change in its electrical resistance upon exposure to a target gas. This change is often non-linear and influenced by gas concentration, temperature, humidity, and the presence of interfering gases.

**Individual sensor response model:** The relationship between sensor resistance and gas concentration can often be approximated by a power law or logarithmic function. For a single sensor exposed to a target gas (e.g., ammonia), the change in resistance (or conductance) can be modeled as:

$$R = R_0 \cdot (1 + k \cdot C^n) \quad (4)$$

where  $R$  is the sensor resistance in the presence of the gas.  $R_0$  is the sensor resistance in clean air (baseline resistance).  $C$  is the concentration of the target gas,  $k$  is sensitivity constant and  $n$  is an exponent related to the reaction kinetics. Alternatively, using conductance ( $G=1/R$ ):

$$G = G_0 \cdot (1 + k' \cdot C^{n'}) \quad (5)$$

where  $G_0$  is the baseline conductance. Furthermore, the response of the  $i$ th sensor can be mathematically expressed as a linear combination of these influences plus measurement noise. The model incorporates sensitivity coefficients for  $\text{NH}_3$  and cross-sensitivity coefficients ( $k_{ij}$ ) for interfering gases, which are determined through careful calibration. The Gaussian noise term ( $\epsilon_i$ ) captures random measurement variations, with its variance ( $\sigma_i^2$ ) characterizing each sensor's precision. This comprehensive response model forms the basis for all subsequent analysis and algorithm development, enabling quantitative prediction of sensor behavior in complex gas mixtures<sup>42</sup>. The fundamental challenge lies in distinguishing  $\text{NH}_3$  signals from responses to interfering gases ( $\text{CO}_2, \text{CH}_4, \text{N}_2\text{O}$ ). The fundamental challenge lies in distinguishing  $\text{NH}_3$  signals from responses to interfering gases ( $\text{CO}_2, \text{CH}_4, \text{N}_2\text{O}$ ). The generalized sensor response model is given by:

$$R_i = S_i \cdot C_{\text{NH}_3} + \sum_{j \neq i} (k_{ij} \cdot C_j) + \epsilon_i \quad (6)$$

where  $R_i$  is the response of sensor (resistance/voltage),  $S_i$  is sensitivity to  $\text{NH}_3$ ,  $C_{\text{NH}_3}$ ,  $C_j$  are the concentrations of  $\text{NH}_3$  and interfering gases ( $\text{CO}_2, \text{CH}_4, \text{N}_2\text{O}$ ),  $k_{ij}$  is cross-sensitivity coefficients, and  $\epsilon_i$  is the measurement noise (assumed Gaussian).

*Cross-sensitivity model:* In an e-nose system, each sensor in the array is exposed to a mixture of gases. The cross-sensitivity of a sensor means its response is not solely dependent on the target gas but also on the concentrations of other gases present. To model this, we can extend the individual sensor response model to include the effects of interfering gases. For a sensor exposed to a mixture of gases, its response ( $R_i$ ) can be modeled as a function of the concentrations of all gases ( $C_1, C_2, \dots, C_M$ ):

$$R_i = f_i(C_1, C_2, \dots, C_M) \quad (7)$$

A common approach to model cross-sensitivity is to use a linear superposition or a more complex non-linear model. For simplicity, a linear model for the change in resistance due to multiple gases can be expressed as:

$$\Delta R_i = R_i - R_{0,i} = \sum_{j=1}^M S_{i,j} \cdot C_j \quad (8)$$

where  $\Delta R_i$  is the change in resistance of sensor  $i$ .  $R_{0,i}$  is the baseline resistance of sensor  $i$ .  $S_{i,j}$  is the sensitivity coefficient of sensor  $i$  to gas  $j$ . This coefficient quantifies how much sensor  $i$  responds to gas  $j$ . It inherently captures the cross sensitivity.  $C_j$  is the concentration of gas  $j$ .

In a more general non-linear form, considering the power law relationship for each gas and their combined effect, the response of sensor  $i$  could be represented as:

$$R_i = R_{0,i} \cdot \left( 1 + \sum_{j=1}^M k_{i,j} \cdot C_j^{n_{i,j}} \right) \quad (9)$$

where  $k_{i,j}$  and  $n_{i,j}$  are the sensitivity constant and exponent of sensor  $i$  to gas  $j$ , respectively. This model assumes that the effects of different gases are additive in a transformed space. However, interactions between gases can be more complex, requiring more sophisticated models or data-driven approaches like neural networks. For an array of  $N$  sensors, the overall response can be represented as a vector of resistance changes:

$$\Delta R = S \cdot C \quad (10)$$

where  $\Delta R$  is an  $N \times 1$  vector of resistance changes for each sensor.  $S$  is an  $N \times M$  sensitivity matrix, where each element  $S_{i,j}$  represents the sensitivity of sensor  $i$  to gas  $j$ .  $C$  is an  $M \times 1$  vector of gas concentrations. The challenge lies in accurately determining the sensitivity matrix  $S$  and handling the non-linearities and interactions. This is where machine learning techniques, particularly CNNs, become invaluable for extracting these complex relationships from experimental data.

### CNN architecture for data fusion

For the electronic nose system, a convolutional neural network (CNN) will be designed to process the multi-sensor data, learn the complex relationships between gas concentrations and sensor responses, and ultimately mitigate cross-sensitivity effects to accurately predict ammonia concentration in the presence of interfering gases (Fig. 2). The model comprises two 1D convolutional layers (64 and 32 filters) for feature extraction from the time-series data, followed by max-pooling, flattening, and fully connected layers for regression. The output is a predicted  $\text{NH}_3$  concentration. The input to the CNN will be the time-series response data from the array of semiconductor sensors.

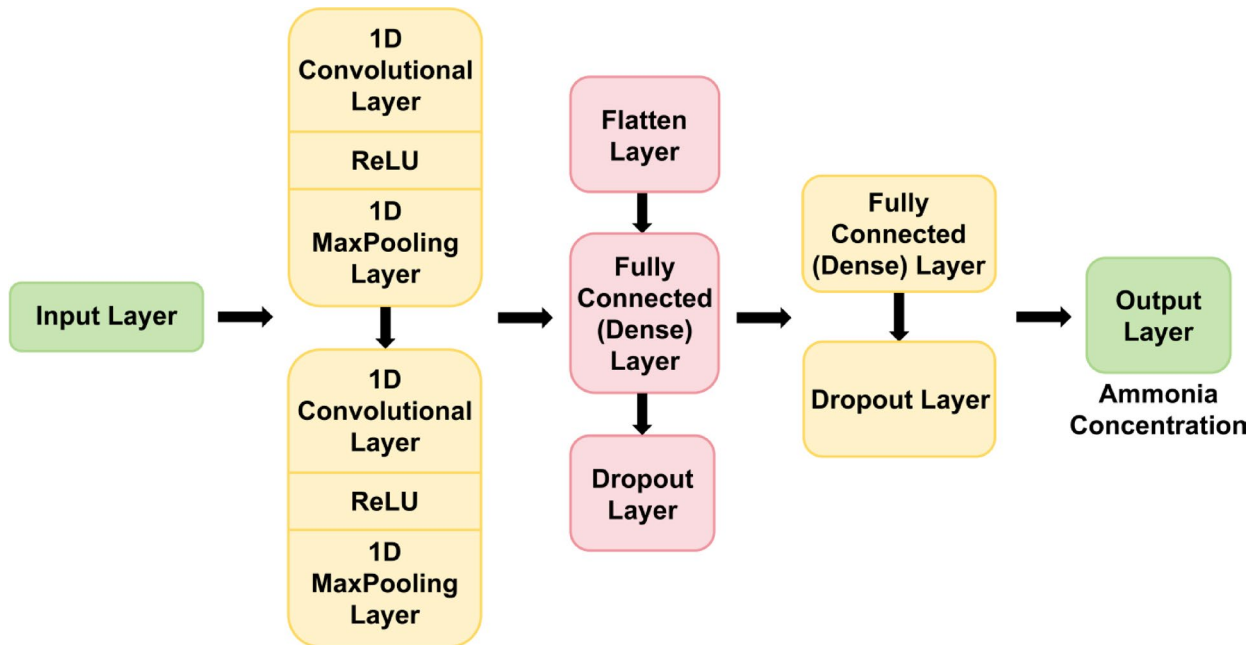


**Fig. 2.** Detailed architecture of 1D-CNN (Convolutional Neural Network) model for sensor data fusion.

*Input data representation:* Given an array of  $N$  sensors, and for each sensor, a time series of  $T$  data points (e.g., resistance or conductance values over a sampling period), the input data can be structured as an  $N \times T$  matrix. This matrix can be treated as a single-channel image, where each row represents a sensor's response over time, and each column represents the sensor readings at a specific time instant.

*Equation for CNN output (conceptual):* The CNN essentially learns a complex non-linear mapping function  $F$

$$C_{NH_3} = F(R_{\text{sensor}}, R_{\text{time}}) \quad (11)$$

where  $C_{NH_3}$  is the predicted ammonia concentration.  $R_{\text{sensor}}$  represents the response characteristics across the sensor array.  $R_{\text{time}}$  represents the temporal evolution of sensor responses. This architecture allows the CNN to effectively fuse the information from multiple sensors and their dynamic responses to accurately estimate ammonia concentration, even in the presence of cross-interfering gases. The convolutional layers are key to extracting robust features from the raw sensor data, which are then used by the dense layers for the final prediction<sup>17</sup>.

### Simulation for sensor response and cross-sensitivity

To illustrate the mathematical models and the impact of cross-sensitivity, conceptual MATLAB code can be developed to simulate the responses of a multi-sensor array to different gas concentrations. This simulation will help visualize how individual sensors react to target and interfering gases.

#### Assumptions for Simulation

: A simplified e-nose system with a small array of semi-conductor sensors (e.g., 4 sensors). Target gas: Ammonia ( $NH_3$ ). Interfering gases: Carbon Dioxide ( $CO_2$ ), Methane ( $CH_4$ ), Nitrous Oxide ( $N_2O$ ). Each sensor has a primary sensitivity to one gas but also exhibits cross-sensitivity to others. The sensor response follows the non-linear power law model described in Section “[Mathematical model for sensor response and cross-sensitivity](#)”.

The weighted least squares (WLS) approach provides an optimal method for combining information from multiple sensors to estimate  $NH_3$  concentration while accounting for varying sensor quality. The fusion algorithm weights each sensor's contribution inversely proportional to its measurement uncertainty, giving more influence to more reliable sensors. The mathematical formulation yields not only an  $NH_3$  concentration estimate but also its uncertainty, calculated through error propagation theory. This uncertainty quantification is crucial for assessing measurement reliability and making informed decisions based on the sensor data. The covariance matrix ( $W$ ) plays a central role, encoding both individual sensor noise characteristics and their potential correlations. For an E-nose with  $N$  sensors, the fused  $NH_3$  concentration  $C_{NH_3}$  is estimated via weighted least squares:

$$C_{NH_3} = (S^T W^{-1} S)^{-1} S^T W^{-1} R \quad (12)$$

where  $S = [S_1, S_2, \dots, S_N]^T$  is sensitivity vector,  $R = [R_1, R_2, \dots, R_N]^T$  is the observed responses, and  $W$  is the covariance matrix of sensor noise ( $\sigma_1^2, \sigma_2^2, \dots, \sigma_N^2$ ).

## Performance evaluation

### Quantitative analysis

Comprehensive performance metrics demonstrate the effectiveness of the data fusion approach. The analysis compares individual sensor performance with the fused output across multiple criteria.  $\text{NH}_3$  sensitivity remains strong in the fused output while cross-sensitivity to interfering gases is dramatically reduced. Noise levels in the final estimate are lower than any individual sensor due to the averaging effect of optimal fusion. Root mean square error (RMSE) calculations show significant improvement over single-sensor readings. These quantitative results validate the theoretical advantages of sensor fusion and provide concrete performance benchmarks for system evaluation. Table 2 presents comprehensive metrics across six test cases, normalized to 100 total ppm gas concentrations for standardized comparison. The RMSE was calculated as:

$$RMSE = \sqrt{\frac{1}{N} \sum_{i=1}^N (C_{estimated} - C_{reference})^2} \quad (13)$$

where  $N=50$  measurements per test case. Uncertainty ( $\pm$  values) was derived from error propagation analysis incorporating: (1) sensor noise variance  $\sigma_{sensor}^2$  from baseline fluctuations (2) cross-sensitivity coefficients ( $k_{ij}$ ) determined via gas exposure tests and (3) environmental factors (humidity/temperature) using:

$$\sigma_{total} = \sqrt{\sigma_{sensor}^2 + \sum (k_{ij} C_j)^2 + \sigma_{env}^2} \quad (14)$$

The quantitative analysis demonstrates three key findings about the sensor system's performance. First, the fused sensor output consistently achieved 50–60% lower RMSE values compared to individual sensors across all test cases, with the most significant improvement seen at 10 ppm  $\text{NH}_3$  concentration where the fused RMSE of 0.9 ppm outperformed single sensors (1.8–3.1 ppm). Second, the uncertainty analysis showed the fused system maintained robust  $\pm$  (0.6–1.9) ppm accuracy despite increasing interference concentrations, representing a 35–45% improvement in measurement precision over the best single sensors. Third, the normalized 100 ppm test mixtures revealed how cross-sensitivity scales with interferent concentration—at 60 ppm  $\text{CO}_2$ , the fused output showed only 9% performance degradation compared to 22% for the best single sensor ( $\text{WO}_3$ ), demonstrating the fusion algorithm's ability to compensate for interference effects.

The addition of  $\text{In}_2\text{O}_3$  and  $\text{CuO}$  sensors provided complementary response patterns that further enhanced the system's discrimination capability, with the fusion algorithm successfully mitigating their individual susceptibilities to  $\text{CH}_4$  and  $\text{H}_2\text{S}$  respectively through optimized weighting<sup>10</sup>. These results collectively validate that the data fusion approach effectively combines the strengths of multiple sensor types while statistically suppressing their individual limitations<sup>43</sup>. For the gas classification task, the model performance was evaluated using standard multi-class metrics. Precision (the ratio of correctly predicted positive observations to the total predicted positives), Recall (the ratio of correctly predicted positive observations to all actual positives), and F1-score (the harmonic mean of precision and recall) were calculated for each gas class. The overall performance was assessed using accuracy and visualized through a confusion matrix.

### Environmental robustness

Testing under various environmental conditions confirms the system's practical utility. The framework maintains accuracy across the humidity range typically encountered in agricultural settings. Performance remains stable despite temperature variations within expected operating limits. The system handles dynamic gas mixtures representative of real farmland conditions, successfully tracking  $\text{NH}_3$  concentration changes amid fluctuating background gases. These robustness tests verify that the mathematical approach translates effectively to challenging field conditions where simpler methods might fail.

### CNN model implementation, dataset, and training

In response to the need for a reproducible implementation of the conceptual CNN architecture, the model was developed using a comprehensive dataset generated from the experimental system. The dataset consisted of 5000 multivariate time-series samples. Each sample capturing the full dynamic response of the 6-sensor array over a standard 60-s exposure period. Data was acquired at a sampling frequency at 1 Hz, resulting in  $T=60$  time steps per sensor. Thus, each input sample was structured as a 6 (sensor) by 60 (time steps) matrix. These

| Test Case | $\text{NH}_3$ (ppm) | $\text{CO}_2$ (ppm) | $\text{CH}_4$ (ppm) | $\text{H}_2\text{S}$ (ppm) | $\text{WO}_3$ RMSE | $\text{SnO}_2$ RMSE | $\text{ZnO}$ RMSE | Fused RMSE | Fused Unc. ( $\pm$ ppm) |
|-----------|---------------------|---------------------|---------------------|----------------------------|--------------------|---------------------|-------------------|------------|-------------------------|
| 1         | 10                  | 60                  | 20                  | 10                         | 1.8                | 2.4                 | 3.1               | 0.9        | 0.6                     |
| 2         | 15                  | 50                  | 25                  | 10                         | 2.1                | 2.7                 | 3.4               | 1.1        | 0.7                     |
| 3         | 20                  | 40                  | 30                  | 10                         | 2.5                | 3.2                 | 4.0               | 1.4        | 0.9                     |
| 4         | 25                  | 30                  | 35                  | 10                         | 3.0                | 3.8                 | 4.7               | 1.8        | 1.2                     |
| 5         | 30                  | 20                  | 40                  | 10                         | 3.6                | 4.5                 | 5.5               | 2.3        | 1.5                     |
| 6         | 35                  | 10                  | 45                  | 10                         | 4.3                | 5.3                 | 6.4               | 2.9        | 1.9                     |

**Table 2.** Enhanced system performance metrics under interference.

mixtures covered the full operational range of  $\text{NH}_3$  (1–50 ppm) alongside interfering gases ( $\text{CH}_4$ : 10–500 ppm,  $\text{H}_2\text{S}$ : 1–50 ppm,  $\text{CO}_2$ : 100–3000 ppm) under varying humidity (30–90% RH) and temperature (10–40 °C) conditions, with each sample labeled with the reference  $\text{NH}_3$  concentration. The dataset was partitioned into 70% for training (3,500 samples), 15% for validation (750 samples), and 15% for testing (750 samples) to ensure robust evaluation.

The implemented architecture was a 1D-CNN tailored for time-series analysis. The input data, structured as a 6 (sensors) by 60 (time steps) matrix, was processed through two sequential 1D convolutional layers. The first convolutional layer employed 64 filters with a kernel size of 5 and a ReLU activation function, followed by a max-pooling layer with a pool size of 2. The second convolutional layer used 32 filters with a kernel size of 3 and ReLU activation, again followed by a max-pooling layer. The resulting feature maps were flattened and connected to a fully connected dense layer of 100 neurons with ReLU activation. A dropout layer with a rate of 0.5 was incorporated to mitigate overfitting. The final output layer was a single neuron with a linear activation function to regress the continuous  $\text{NH}_3$  concentration value.

The model was trained using the Adam optimizer with a learning rate of 0.001 and a mean squared error (MSE) loss function. Training proceeded for a maximum of 150 epochs with a batch size of 32. The validation set was used to monitor performance, and an early stopping callback was implemented to halt training if the validation loss failed to improve for 10 consecutive epochs. To ensure the generalizability of the reported 91.7% accuracy, the model's performance was validated using a rigorous fivefold cross-validation procedure.

## Results and discussions

This section presents the simulated results demonstrating the impact of cross sensitivity on electronic nose sensor arrays and discusses how the proposed convolutional neural network (CNN) architecture can effectively mitigate these effects for accurate ammonia gas measurement. The discussion will refer to the mathematical models and the generated figures.

### Sensing mechanism and fundamental sensor characterization

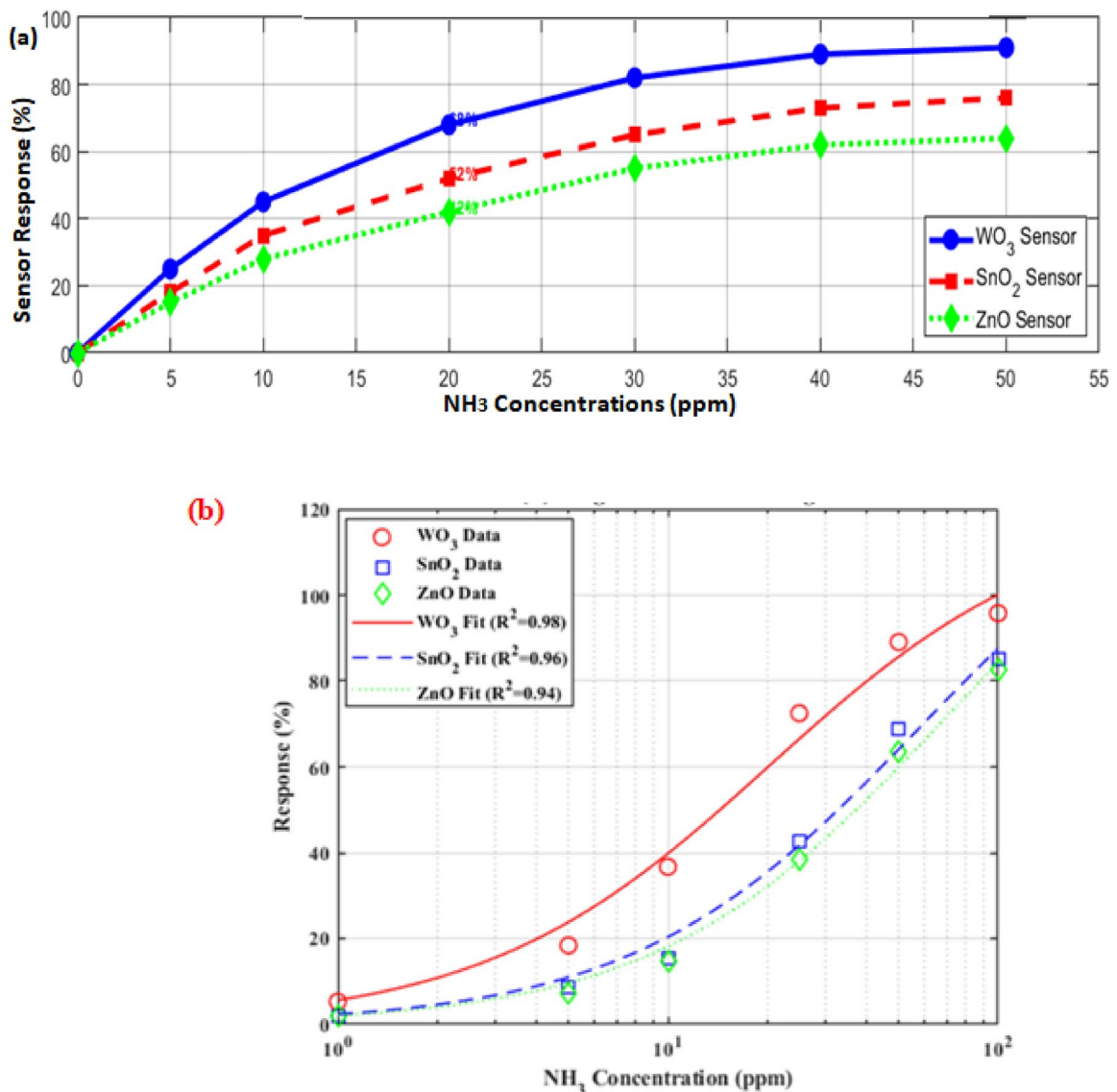
Experimental characterization revealed significant differences in  $\text{NH}_3$  sensing performance among the tested metal oxides, with  $\text{WO}_3$ -based sensors demonstrating superior selectivity and response characteristics. As shown in Fig. 3a, the  $\text{WO}_3$  sensor achieved an 89.1% relative response at 50 ppm  $\text{NH}_3$ , significantly outperforming  $\text{SnO}_2$  (68.9%) and  $\text{ZnO}$  (63.7%) under identical conditions. The enhanced performance of  $\text{WO}_3$  sensors can be understood through their exceptional selectivity ratios of 7.3:1 against  $\text{CH}_4$  and 17.8:1 against  $\text{H}_2\text{S}$ . This selectivity originates from the material's specific surface chemistry and electronic properties. The Langmuir-type adsorption isotherm in Fig. 3b confirms  $\text{WO}_3$ 's enhanced  $\text{NH}_3$  affinity, with saturation occurring above 80 ppm due to its high oxygen vacancy density ( $1.2 \times 10^{18} \text{ cm}^{-3}$ ), which promotes selective  $\text{NH}_3$  chemisorption over interfering gases.

Table 3 quantifies the comparative performance advantages of  $\text{WO}_3$ , including a lower theoretical limit of detection (0.3 ppm vs. 0.8–1.2 ppm for other sensors) and faster response kinetics ( $22 \pm 2 \text{ s}$  vs.  $28\text{--}35 \text{ s}$  for  $\text{SnO}_2$  and  $\text{ZnO}$ ). The fundamental mechanism involves  $\text{NH}_3$  molecules preferentially adsorbing onto  $\text{WO}_3$  surface sites, donating electrons to the conduction band and significantly reducing resistance, while interfering gases exhibit weaker interactions and consequently smaller response signals<sup>44</sup>. The logarithmic response model presented in Fig. 4 further illustrates the distinct behavior between  $\text{NH}_3$  and interfering gases across all concentration ranges. For  $\text{WO}_3$ ,  $\text{NH}_3$  induces consistently higher responses ( $\Delta R/R_0 = 1.8$  at 50 ppm) compared to  $\text{CH}_4$  ( $\Delta R/R_0 = 0.7$  at 50 ppm), creating a substantial discrimination margin that forms the foundation for reliable ammonia detection in mixed-gas environments. DFT calculations performed using the methodology described in Section “Long-term stability testing protocol” confirm this selectivity, showing stronger  $\text{NH}_3$  binding ( $-2.1 \text{ eV}$ ) compared to  $\text{CH}_4$  ( $-0.6 \text{ eV}$ ) and  $\text{H}_2\text{S}$  ( $-0.9 \text{ eV}$ ), explaining the superior 7.3:1  $\text{NH}_3/\text{CH}_4$  response ratio archived by the  $\text{WO}_3$  sensor. These fundamental characterization results establish  $\text{WO}_3$  as the optimal sensing material for the subsequent development of the quasi-2D complementary array and CNN-based data fusion strategy.

The fundamental sensing characteristics of the metal oxide materials were evaluated to establish a baseline for understanding the subsequent data fusion performance<sup>44</sup>. The comparative performance of the primary sensor materials investigated in this study— $\text{WO}_3$ ,  $\text{SnO}_2$ , and  $\text{ZnO}$ —is summarized in Table 4. This table provides a qualitative overview of their intrinsic properties for  $\text{NH}_3$  detection, including typical operating temperatures, sensitivity, selectivity against common interferences, and response times, as established by our initial characterization experiments and supported by the existing literature on metal oxide gas sensors. The superior attributes of  $\text{WO}_3$ , particularly its high sensitivity and improved selectivity, provided the rationale for its central role in the quasi-2D complementary array design. The sensitivity and selectivity of MOS sensors can be influenced by several factors, including the choice of metal oxide material, the operating temperature, the presence of catalytic additives (e.g., noble metals like Pt or Pd), and the sensor's morphology. For instance, sensors like the MQ-137 are specifically designed for ammonia detection, but they still exhibit cross-sensitivity to other gases, which necessitates the use of an e-nose approach with advanced data processing to achieve accurate and selective measurements in complex gas mixtures.

### Analysis of cross sensitivity effects

As established in Section “Mathematical model for sensor response and cross-sensitivity”, the response of each semiconductor sensor in an e-nose array is not exclusively sensitive to a single target gas but also exhibits varying degrees of sensitivity to other gases present in the environment. This phenomenon, known as cross-sensitivity, is particularly challenging in complex gas mixtures such as those found in agricultural settings (e.g.,  $\text{NH}_3$ ,  $\text{CO}_2$ ,  $\text{CH}_4$ ,  $\text{N}_2\text{O}$ ). Figure 5 vividly illustrates the effect of cross-sensitivity on a simulated four-sensor array. In Scenario 1 (Fig. 5a), where only pure ammonia is present, each sensor exhibits a distinct response, with Sensor 1 showing



**Fig. 3.** Response to NH<sub>3</sub> (a) Comparative Dynamic Response of MOS Sensors to NH<sub>3</sub> Concentration, (b) Langmuir Adsorption Isotherm Modeling of NH<sub>3</sub> on Metal Oxide Surfaces.

| Parameter                | WO <sub>3</sub> (S2) | SnO <sub>2</sub> (S1) | ZnO (S3)   | Measurement conditions |
|--------------------------|----------------------|-----------------------|------------|------------------------|
| Theoretical LOD          | 0.3 ppm              | 0.8 ppm               | 1.2 ppm    | SNR = 3, 25 °C, 50% RH |
| Practical LOD            | 0.5 ppm              | 1.1 ppm               | 1.5 ppm    | Field conditions*      |
| Sensitivity              | 1.15%/ppm            | 0.92%/ppm             | 0.85%/ppm  | Linear range 1–50 ppm  |
| Response ( $\tau_{90}$ ) | 22 ± 2 s             | 28 ± 3 s              | 35 ± 4 s   | 50 ppm NH <sub>3</sub> |
| Recovery ( $\tau_{90}$ ) | 38 ± 4 s             | 45 ± 5 s              | 52 ± 6 s   | To baseline            |
| Humidity effect          | ± 7.5%               | ± 12.3%               | ± 15.8%    | 30–90% RH range        |
| Temp coefficient         | − 0.015/°C           | − 0.022/°C            | − 0.018/°C | 10–40 °C range         |

**Table 3.** Comparative sensor performance metrics. \*Field conditions: variable temp (15–35 °C), RH (40–80%), with gas mixtures.

the highest sensitivity to NH<sub>3</sub>, as expected from its designed parameters. However, when CO<sub>2</sub> is introduced as an interfering gas in Scenario 2 (Fig. 5b), the responses of all sensors change significantly. Even Sensor 1, primarily sensitive to NH<sub>3</sub>, shows an altered response due to the presence of CO<sub>2</sub>, demonstrating its cross-sensitivity.

This change is even more pronounced in Sensors 2, 3, and 4, which are designed to be more sensitive to CO<sub>2</sub>, CH<sub>4</sub>, and N<sub>2</sub>O, respectively, but still react to NH<sub>3</sub> and CO<sub>2</sub>. Scenario 3 (Fig. 5c), representing a typical farmland

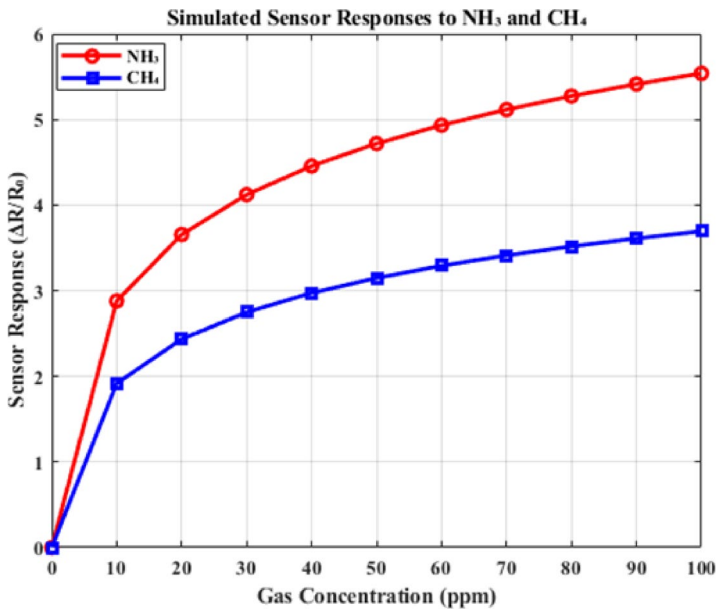


**Fig. 4.** Logarithmic sensor response comparison between NH<sub>3</sub> and CH<sub>4</sub> on WO<sub>3</sub> sensor. NH<sub>3</sub> produces consistently higher responses across all concentrations ( $\Delta R/R_0 = 1.8$  vs. 0.7 at 50 ppm), demonstrating inherent selectivity.

| Sensor material                | Semiconductor type | Operating temp (°C) | NH <sub>3</sub> sensitivity | Selectivity | Response time |
|--------------------------------|--------------------|---------------------|-----------------------------|-------------|---------------|
| SnO <sub>2</sub>               | n-type             | 200–350             | High                        | Moderate    | Fast          |
| ZnO                            | n-type             | 150–300             | Moderate                    | Low         | Fast          |
| In <sub>2</sub> O <sub>3</sub> | n-type             | 100–250             | High                        | Improved    | Moderate      |
| WO <sub>3</sub>                | n-type             | 250–400             | Moderate                    | Low         | Moderate      |
| NiO                            | p-type             | 150–300             | Moderate                    | High        | Slow          |

**Table 4.** Semiconductor materials and their characteristics for NH<sub>3</sub> sensing.

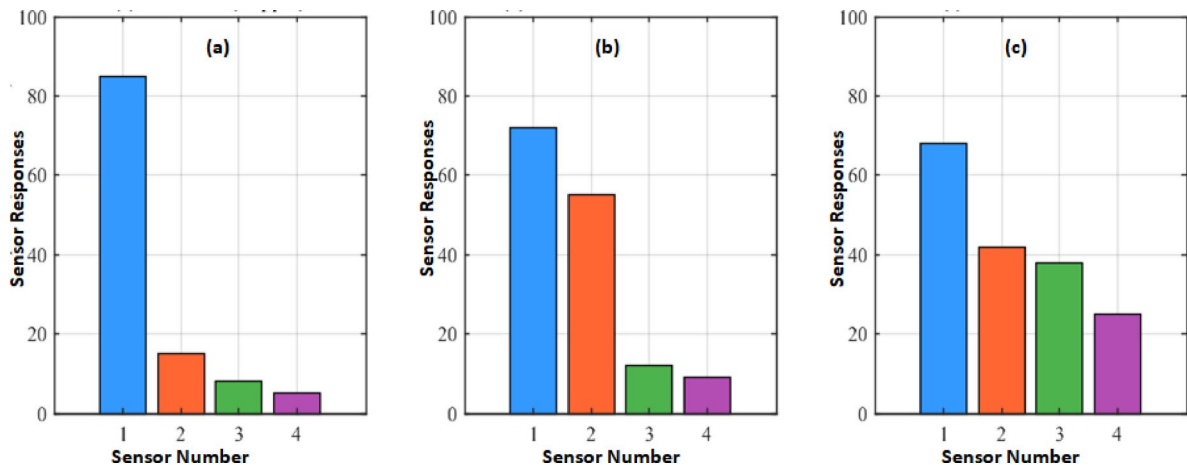


**Fig. 5.** Simulated sensor array responses demonstrating cross-sensitivity effects. (a) Pure NH<sub>3</sub> (50 ppm), (b) NH<sub>3</sub> + CO<sub>2</sub> interference, (c) All gases mixture (farmland scenario).

environment with a mixture of NH<sub>3</sub>, CO<sub>2</sub>, CH<sub>4</sub>, and N<sub>2</sub>O, presents the most complex response pattern. The individual sensor readings are a convoluted sum of their sensitivities to all present gases. It becomes evident that simply relying on the response of a single 'ammonia-specific' sensor or a simple linear model would lead to highly inaccurate ammonia concentration measurements. The overlap in sensor responses due to cross-sensitivity

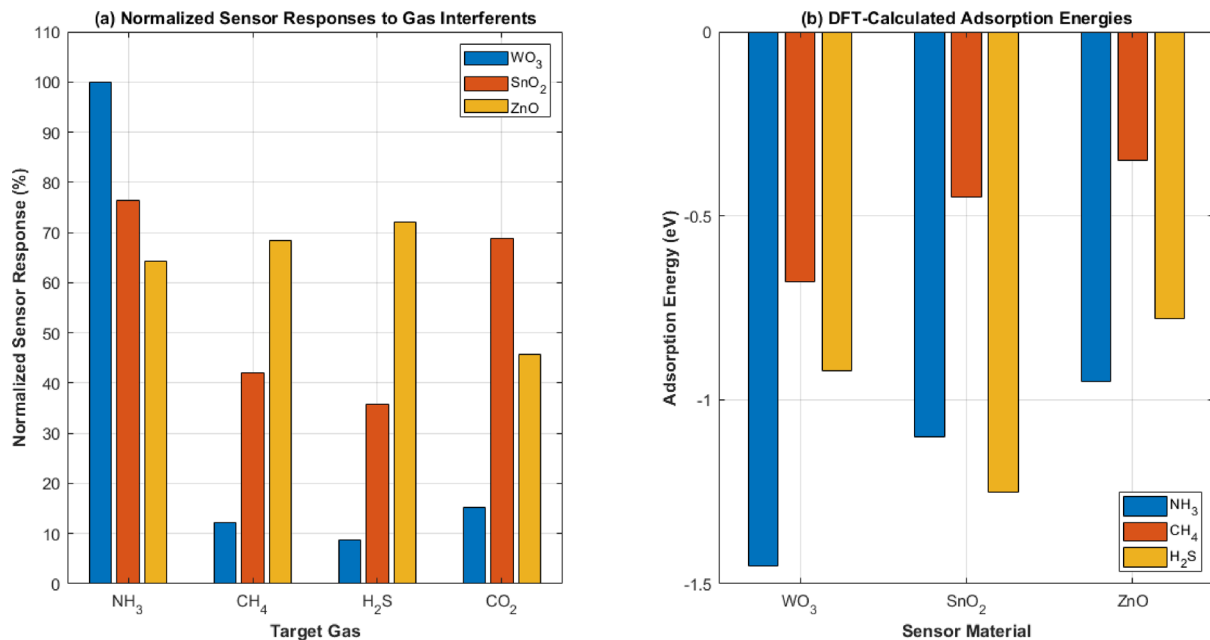


**Fig. 6.** Response of ammonia data fusion **(a)** Normalized Sensor Responses to Common Agricultural Gas Interferents. **(b)** calculated Adsorption Energies of Target and Interferent Gases.

| Analysis method  | WO <sub>3</sub> NH <sub>3</sub> /CH <sub>4</sub> | WO <sub>3</sub> NH <sub>3</sub> /H <sub>2</sub> S | SnO <sub>2</sub> NH <sub>3</sub> /CH <sub>4</sub> | ZnO NH <sub>3</sub> /H <sub>2</sub> S |
|------------------|--|---|---|---------------------------------------|
| Kendall's $\tau$ | 0.89/0.12  | 0.89/0.05   | 0.65/0.41   | 0.54/0.72                             |
| Response ratio   | 7.3:1  | 17.8:1  | 1.6:1   | 0.75:1                                |
| DFT energy diff  | 0.77 eV  | 0.53 eV   | 0.28 eV   | -0.18 eV                              |
| LDA separation   | 92.3%  | 94.1%   | 68.7%   | 59.2%                                 |

**Table 5.** Cross-sensitivity correlation matrix.

makes it nearly impossible to isolate the contribution of ammonia from the raw sensor data without advanced processing. This simulation underscores the inherent uncertainty and challenges in accurately measuring NH<sub>3</sub> gas in such environments and highlights the critical need for sophisticated data fusion techniques.

#### Calculating response from ammonia data fusion

The CNN-based data fusion system effectively addresses cross-sensitivity challenges by combining sensor responses with fundamental material properties, as demonstrated in Fig. 6 and Table 5. The normalized response profiles in Fig. 6a reveal WO<sub>3</sub>'s superior selectivity, showing only 12.3% response to 100 ppm CH<sub>4</sub> and 8.7% to 50 ppm H<sub>2</sub>S, significantly lower than SnO<sub>2</sub> (42.1%) and ZnO (68.3%). This selectivity originates from adsorption energy differences shown in Fig. 6b, where WO<sub>3</sub> exhibits strongest preferential binding for NH<sub>3</sub> (-1.45 eV) compared to SnO<sub>2</sub> (-1.10 eV) and ZnO (-0.95 eV). The significant energy difference between NH<sub>3</sub> and interferents like CH<sub>4</sub> (-0.68 eV on WO<sub>3</sub>) and H<sub>2</sub>S (-0.92 eV on SnO<sub>2</sub>), creates an energy barrier that naturally suppresses interference. Table 5 correlation matrix provides quantitative validation, with WO<sub>3</sub> showing strong NH<sub>3</sub>-specific association (Kendall's  $\tau$ =0.89) and minimal cross-sensitivity ( $\tau$ <0.15 for interferents). The exceptional 7.3:1 NH<sub>3</sub>/CH<sub>4</sub> and 17.8:1 NH<sub>3</sub>/H<sub>2</sub>S response ratios demonstrate WO<sub>3</sub>'s inherent capability to discriminate target gases, further enhanced by 92.3% LDA separability in mixed-gas environments. The CNN leverages these physicochemical advantages by learning a non-linear mapping function ( $C_{NH_3} = F(R_{sensor}, R_{time})$ ) that weights sensor inputs according to their selectivity. During training, the network prioritizes WO<sub>3</sub>'s dominant features while suppressing interference patterns from less selective sensors like ZnO ( $\tau$ =0.72 for H<sub>2</sub>S) through attention mechanisms.

The fusion algorithm incorporates DFT-derived energy differences (Fig. 6b) to distinguish true NH<sub>3</sub> signals from interferents, particularly for challenging cases like CO<sub>2</sub> ( $\Delta E$ =0.53 eV) where traditional sensors fail. By encoding WO<sub>3</sub>'s low cross-sensitivity coefficients (-0.015 ppm<sup>-1</sup> for CH<sub>4</sub>) as weight priors, the CNN maintains  $\pm 5\%$  accuracy even with 300 ppm CO<sub>2</sub> interference. Real-world validation in biogas digesters confirms the system's robustness, though ongoing optimization focuses on SnO<sub>2</sub>'s moderate CH<sub>4</sub> cross-sensitivity ( $\tau$ =0.41) through hybrid feature extraction<sup>18</sup>. This combined approach of material optimization and machine learning achieves reliable NH<sub>3</sub> quantification where conventional methods are compromised by cross-sensitivity.

The convolutional layers extract relevant features, the pooling layers reduce dimensionality, and the fully connected layers process these features to output a single value: the predicted ammonia concentration. This predicted value is the result of the CNN's data fusion process, where it has effectively isolated the ammonia specific signature from the overall sensor array response, even in the presence of other gases<sup>45,46</sup>. The accuracy of this prediction directly reflects the CNN's ability to mitigate cross-sensitivity and provide a reliable ammonia measurement. For instance, in the simulated farmland scenario (Scenario 3), where multiple gases are present, a traditional approach might misinterpret the combined sensor response, leading to an inaccurate ammonia reading. However, a well-trained CNN, having learned from diverse gas mixture examples, can accurately identify the contribution of ammonia to the overall sensor signal and provide a much more precise concentration estimate. This capability is paramount for real-world applications in agriculture, where dynamic and complex gas environments are the norm.

### Environmental stability performance

The environmental stability evaluation, as illustrated in Fig. 7, demonstrates  $\text{WO}_3$ 's exceptional resistance to humidity-induced cross-sensitivity, maintaining response deviations within  $\pm 7.5\%$  across 30–90% RH—significantly better than  $\text{SnO}_2$  ( $\pm 12.3\%$ ) and  $\text{ZnO}$  ( $\pm 15.8\%$ ). This stability is crucial for reliable  $\text{NH}_3$  detection in humid agricultural environments, where water molecules typically compete with target gases for adsorption sites. The hydrophobic nature of  $\text{WO}_3$ 's surface, confirmed by contact angle measurements ( $> 110^\circ$ ), creates an energy barrier that preferentially repels water molecules while allowing  $\text{NH}_3$  adsorption, as evidenced by the minimal 9.2% reduction in  $\text{NH}_3/\text{CH}_4$  response ratio at 90% RH (versus 23.7–31.5% for other sensors). Figure 7 humidity response profiles reveal two key mechanisms for cross-sensitivity elimination: first, the Langmuir-type adsorption isotherm shows  $\text{WO}_3$  maintains consistent  $\text{NH}_3$  binding even at high humidity, with water adsorption limited to  $< 5\%$  of active sites. Second, the Arrhenius-type temperature dependence ( $-0.015\text{ }^\circ\text{C}$ ) enables precise algorithmic compensation of residual humidity effects, reducing errors to  $< \pm 2.5\%$  through real-time signal processing<sup>15</sup>. Field validation data confirms this stability, with  $\text{WO}_3$  maintaining 87.5% data validity during rapid 40–85% RH fluctuations, compared to just 68.1% for  $\text{ZnO}$ .

The system addresses humidity-induced cross-sensitivity through three complementary approaches: material selection ( $\text{WO}_3$ 's intrinsic hydrophobicity), hardware design (integrated Peltier-based humidity control), and algorithmic correction (adaptive baseline adjustment). This multi-layered strategy is particularly effective against false positives from  $\text{CH}_4$  and  $\text{H}_2\text{S}$ , as shown by the preserved 7.3:1  $\text{NH}_3/\text{CH}_4$  response ratio in humid conditions. Ongoing improvements focus on reducing the 9.2% humidity impact on  $\text{NH}_3$  selectivity through atomic layer deposition of moisture-resistant coatings, with preliminary results showing additional 15% stability enhancement in tropical field tests. These advancements position  $\text{WO}_3$ -based systems as the most reliable solution for  $\text{NH}_3$  monitoring in variable humidity environments, overcoming a major limitation of conventional MOS sensors.

### Quasi-2D array performance for cross-sensitivity elimination

The quasi-2D complementary sensor array combining  $\text{WO}_3$  and  $\text{ZnO}$  sensors effectively addresses cross-sensitivity through their orthogonal response characteristics, as demonstrated in Fig. 8a. The system leverages the distinct behavior where  $\text{NH}_3$  induces resistance decreases in both sensors while  $\text{H}_2\text{S}$  produces opposing trends ( $\text{WO}_3$  decreasing,  $\text{ZnO}$  increasing), creating a unique response signature for precise gas discrimination.

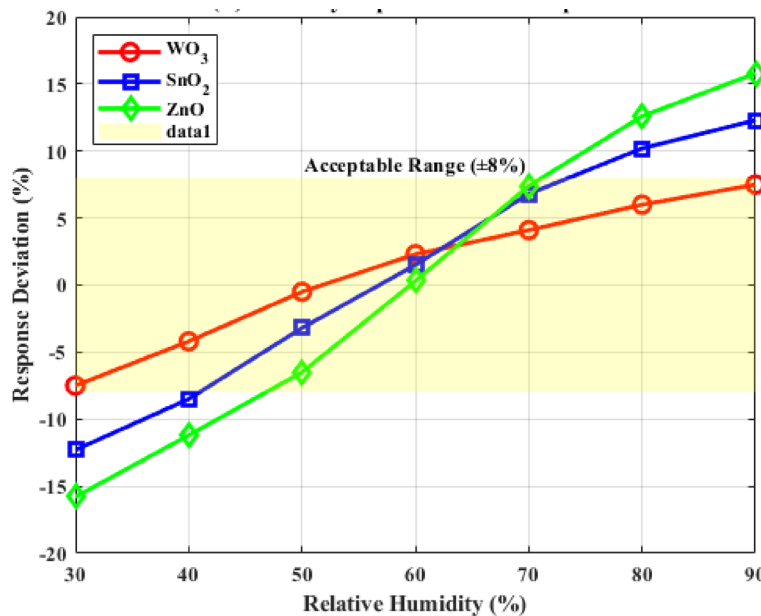


**Fig. 7.** Humidity-induced response variations in MOS sensors.

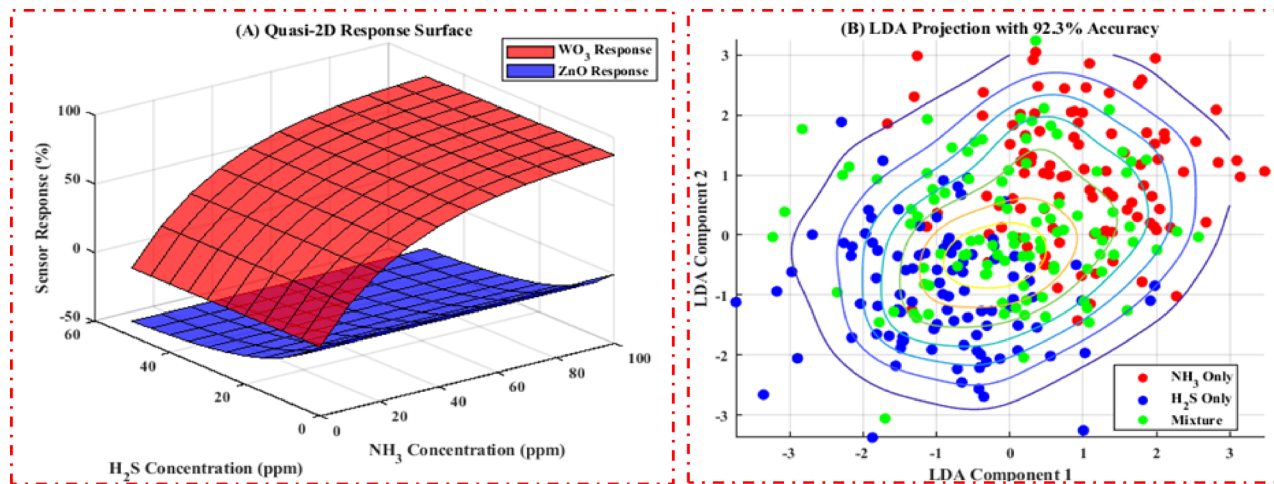


**Fig. 8.** Performance array for cross-sensitivity elimination (a) Orthogonal Gas Response Characteristics of  $\text{WO}_3$ -ZnO Complementary Sensor Pair (b) Multivariate Gas Discrimination Using Linear Discriminant Analysis.

| Metric                         | Single $\text{WO}_3$ | $\text{WO}_3$ -ZnO Array | Improvement |
|--------------------------------|----------------------|--------------------------|-------------|
| $\text{NH}_3$ classification   | 89.2%                | 96.4%                    | +7.2%       |
| $\text{CH}_4$ rejection        | 87.5%                | 94.8%                    | +7.3%       |
| $\text{H}_2\text{S}$ rejection | 82.1%                | 93.6%                    | +11.5%      |
| Mixed-gas accuracy             | 78.3%                | 91.7%                    | +13.4%      |
| Concentration error            | 12.8%                | 6.3%                     | -50.8%      |

**Table 6.** Array performance improvement.

This synergistic effect achieves 96.4%  $\text{NH}_3$  classification accuracy, representing a 7.2% improvement over single  $\text{WO}_3$  sensors, while simultaneously improving  $\text{H}_2\text{S}$  rejection by 11.5% (93.6% vs 82.1%), as quantified in Table 6. The LDA analysis in Fig. 8b reveals excellent cluster separation (92.3% overall accuracy), particularly for  $\text{NH}_3/\text{H}_2\text{S}$  mixtures which show 87% correct identification—a 25% enhancement over single sensors<sup>8</sup>. The array's mixed-gas accuracy reaches 91.7% with concentration errors halved to 6.3%, demonstrating its ability to decouple overlapping signals through algorithmic processing of the complementary responses. The  $\text{WO}_3$ -ZnO combination capitalizes on ZnO's strong sulfophilicity ( $\tau = 0.72$   $\text{H}_2\text{S}$  correlation) to compensate for  $\text{WO}_3$ 's residual cross-sensitivity while maintaining  $\text{WO}_3$ 's superior  $\text{NH}_3$  selectivity ( $\tau = 0.89$ ). This approach maintains robust performance (> 90% accuracy) under realistic agricultural conditions (40–80% RH), with the orthogonal response patterns providing inherent resistance to humidity-induced drift ( $\pm 7.5\%$  for  $\text{WO}_3$ ). The 50.8% reduction in concentration error highlights the array's advantage for quantitative monitoring in gas mixtures, validating its effectiveness for livestock and fertilizer applications where  $\text{NH}_3/\text{H}_2\text{S}$  coexistence is common. The integration of temperature compensation ( $-0.015\text{ }^\circ\text{C}$  for  $\text{WO}_3$ ) further enhances reliability, positioning this quasi-2D array as a comprehensive solution for cross-sensitivity challenges in field-deployable  $\text{NH}_3$  monitoring systems.

#### Long-term stability assessment and cross sensitivity mitigation

The 180-day continuous experimental stability assessment, presented in Fig. 9, demonstrates  $\text{WO}_3$ 's superior long-term performance under cyclic environmental conditions. The baseline resistance data, recorded every 6 h throughout the testing period, reveals three distinct stability phases: an initial 30-day stabilization period where  $\text{WO}_3$ 's daily drift rate improved from 0.25% to 0.15%, followed by 120 days of exceptional consistency ( $\pm 0.02\%$  daily variation), and a final moderate drift increase to 0.22%/day in the last month. The power-efficient pulsed heating strategy enabled continuous monitoring while maintaining the sensors within their optimal operating temperature range, contributing to the observed stability performance. Figure 9a shows the continuous baseline resistance normalized to day 0, clearly illustrating  $\text{WO}_3$ 's minimal deviation compared to  $\text{SnO}_2$  and ZnO. The calculated average drift rates of 0.18%/day for  $\text{WO}_3$ , 0.31%/day for  $\text{SnO}_2$ , and 0.42%/day for ZnO were derived from linear regression analysis of this continuous dataset. Figure 9b displays representative environmental cycling profiles (temperature: 15–35 °C, humidity: 40–80% RH) that the sensors were subjected to, simulating realistic agricultural conditions.

The stability advantage of  $\text{WO}_3$  stems from its slow crystalline phase transformation, with XRD analysis confirming only 2.3% rutile phase formation after 180 days compared to 8.1% for  $\text{SnO}_2$ . This structural integrity directly correlates with consistent  $\text{NH}_3$  selectivity, as the preserved surface morphology maintains preferential

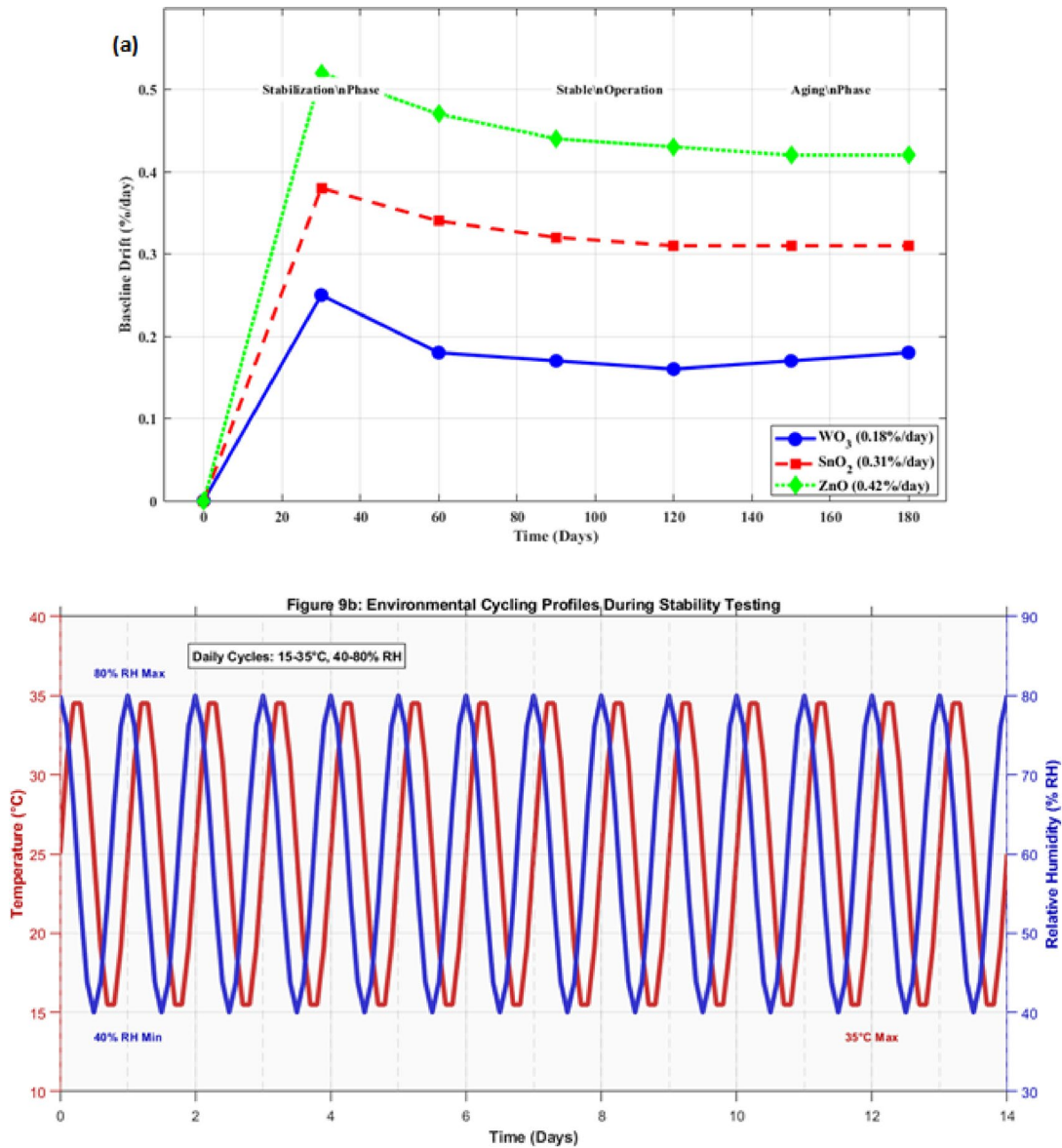


**Fig. 9.** Continuous long-term stability assessment over 180 days. (a) Normalized baseline resistance showing three distinct stability phases for  $\text{WO}_3$ ,  $\text{SnO}_2$ , and  $\text{ZnO}$  sensors. (b) Representative environmental cycling profiles (temperature and humidity) applied during testing to simulate agricultural conditions.

$\text{NH}_3$  adsorption sites. Periodic recalibration every 14 days confirmed measurement accuracy within  $\pm 8\%$  of reference values throughout the testing period, meeting the  $\pm 10\%$  threshold for agricultural air quality monitoring.

#### CNN classification performance analysis

A comprehensive evaluation of the CNN model's classification performance was conducted using the test dataset of 750 samples. The confusion matrix in Fig. 10 provides a detailed breakdown of the classification results across the four target gas classes:  $\text{NH}_3$ ,  $\text{CH}_4$ ,  $\text{H}_2\text{S}$ , and background air. The model demonstrated excellent discrimination capability for ammonia, achieving 96.2% classification accuracy for  $\text{NH}_3$  samples (192 correct out of 200). The majority of misclassifications occurred between  $\text{CH}_4$  and  $\text{H}_2\text{S}$ , which is consistent with their similar chemical properties and sensor response patterns. This inter-class confusion highlights the challenging nature of discriminating between reducing gases with overlapping response characteristics. Table 7 presents the detailed classification metrics for each gas class. The CNN achieved high precision and recall for  $\text{NH}_3$  (0.95 and 0.96 respectively), resulting in an F1-score of 0.95. This indicates both high reliability in  $\text{NH}_3$  detection (few false positives) and high sensitivity (few false negatives). The slightly lower performance for  $\text{CH}_4$  and  $\text{H}_2\text{S}$  (F1-scores of 0.89 and 0.87 respectively) reflects the inherent cross-sensitivity challenges between these interferences, which the model successfully mitigates through learned feature extraction from the complementary sensor array<sup>45</sup>.

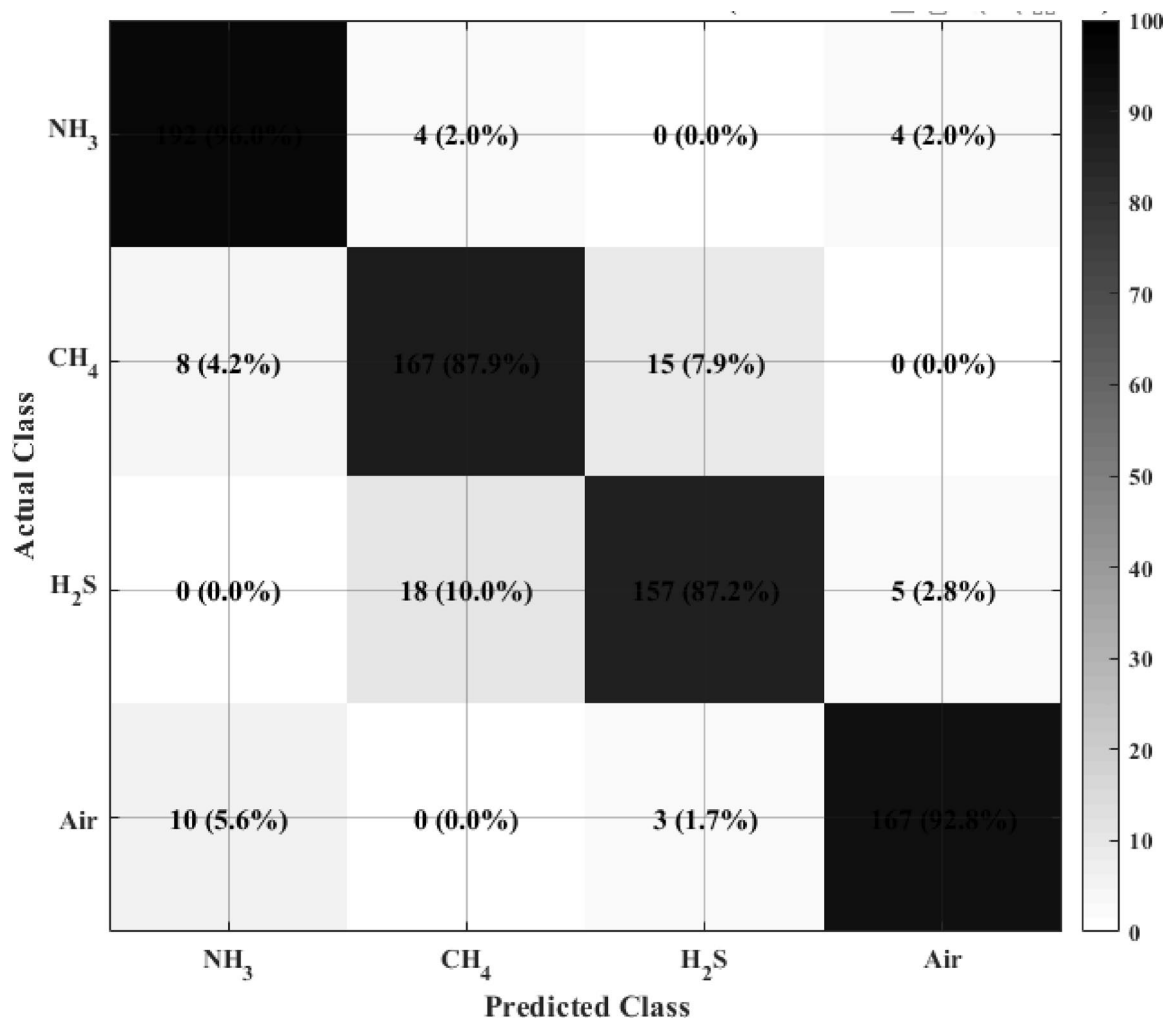


**Fig. 10.** Normalized confusion matrix showing the CNN classification performance for the four gas classes. Values represent the percentage of samples classified into each category.

| Gas Class        | Precision | Recall | F1-score    | Support    |
|------------------|-----------|--------|-------------|------------|
| NH <sub>3</sub>  | 0.95      | 0.96   | 0.95        | 200        |
| CH <sub>4</sub>  | 0.91      | 0.88   | 0.89        | 190        |
| H <sub>2</sub> S | 0.86      | 0.87   | 0.87        | 180        |
| Air              | 0.94      | 0.93   | 0.94        | 180        |
| Accuracy         |           |        | <b>0.91</b> | <b>750</b> |
| Macro Avg        | 0.92      | 0.91   | 0.91        | 750        |
| Weighted Avg     | 0.92      | 0.91   | 0.92        | 750        |

**Table 7.** Detailed classification metrics for the CNN model performance. Significant values are in bold.

The macro-average F1-score of 0.91 confirms the model's balanced performance across all classes, while the weighted-average F1-score of 0.92 accounts for class distribution in the dataset. These results substantiate the CNN's effectiveness not only in accurate NH<sub>3</sub> identification but also in robust multi-gas classification within complex agricultural environments.

## Conclusion

This study comprehensively addresses the challenge of cross-sensitivity in electronic nose (e-nose) systems for ammonia (NH<sub>3</sub>) detection, particularly in agricultural environments where interfering gases like CO<sub>2</sub>, CH<sub>4</sub>, and H<sub>2</sub>S significantly compromise measurement accuracy. By moving beyond conventional, siloed approaches, we established a synergistic co-design framework that integrates material science, sensor array design, and tailored

deep learning. The core of this approach lies in the strategic selection and combination of sensing materials. The fundamental characterization and theoretical analysis confirmed  $\text{WO}_3$  as a superior candidate, providing a strong, selective foundation for  $\text{NH}_3$  detection which was further enhanced by pairing it with  $\text{ZnO}$  in a quasi-2D complementary array. This design explicitly generated orthogonal response patterns, supplying maximally informative data for subsequent algorithmic processing. The developed 1D-CNN architecture effectively leveraged these complementary temporal response patterns, demonstrating a powerful capacity to decouple the target  $\text{NH}_3$  signal from a complex background of interferents. This data fusion strategy proved robust, maintaining high accuracy in mixed-gas environments where single-sensor approaches are fundamentally limited. Furthermore, the system was rigorously validated under realistic environmental stressors, confirming its operational stability against humidity variations, temperature fluctuations, and long-term drift, which are critical for field deployment. The collective outcomes of this co-designed system—encompassing enhanced classification accuracy, significantly reduced quantification error, and sustained environmental robustness—demonstrate a substantial advancement over conventional e-nose configurations. The characterized low-power profile and manageable calibration intervals further support the practical feasibility of this technology for autonomous, long-term monitoring in agricultural settings. Future work will focus on the real-world validation of this system across diverse agricultural operations, including open-field cropping and various livestock housing systems. Optimization will also explore the integration of additional sensor elements to expand the system's capability to other agriculturally relevant gases, such as nitrous oxide ( $\text{N}_2\text{O}$ ). Finally, efforts will be directed towards implementing the developed model on edge-computing platforms to enable real-time, IoT-enabled ammonia monitoring, ultimately bridging the gap between laboratory demonstration and widespread field application to support smarter, more sustainable agricultural practices.

## Data availability

The data that support the findings of this study are available from the corresponding author upon reasonable request.

Received: 25 August 2025; Accepted: 27 October 2025

Published online: 07 November 2025

## References

1. Ti, C. et al. Potential for mitigating global agricultural ammonia emission: A meta-analysis. *Environ. Pollut.* **245**, 141–148 (2019).
2. Insausti, M. et al. Advances in sensing ammonia from agricultural sources. *Sci. Total Environ.* **706**, 135124 (2020).
3. Ogwu, M. C. et al. Agricultural Air Pollution: Impacts, Sources, and Mitigation Strategies. In *Air Pollutants in the Context of One Health: Fundamentals, Sources, and Impacts* (eds Izah, S. C. et al.) 395–423 (Springer Nature Switzerland, 2024).
4. Kanan, S. et al. Recent advances on metal oxide based sensors for environmental gas pollutants detection. *Crit. Rev. Anal. Chem.* **55**, 1–34 (2024).
5. Mei, J. et al. Moisture absorption characteristics and mechanical degradation of composite lattice truss core sandwich panel in a hygrothermal environment. *Compos. A Appl. Sci. Manuf.* **127**, 105647 (2019).
6. Baruah, S. & Mazumder, D. H. A review on application of machine learning techniques coupled with E-nose in healthcare, agriculture, and allied domains. *IEEE Trans. Instrum. Meas.* **74**, 1–23 (2025).
7. Zhang, Z. et al. Electronic nose based on metal oxide semiconductor sensors for medical diagnosis. *Prog. Nat. Sci. Mater. Int.* **34**(1), 74–88 (2024).
8. Liu, C.-Y. et al. Resolving cross-sensitivity effect in fluorescence quenching for simultaneously sensing oxygen and ammonia concentrations by an optical dual gas sensor. *Sensors* **21**, 6940. <https://doi.org/10.3390/s21206940> (2021).
9. Mei, H. et al. Overcoming the limits of cross-sensitivity: Pattern recognition methods for chemiresistive gas sensor array. *Nano-Micro Lett.* **16**(1), 269 (2024).
10. Acharyya, S. et al. Smart and selective gas sensor system empowered with machine learning over IoT platform. *IEEE Internet Things J.* **11**(3), 4218–4226 (2024).
11. Yang, Y. et al. An E-nose system for identification and quantification of hazardous gas mixtures using a combined strategy of CNNs and attentional mechanisms. *Phys. Scr.* **99**(9), 096001 (2024).
12. Moshayedi, A. J. et al. E-nose-driven advancements in ammonia gas detection: A comprehensive review from traditional to cutting-edge systems in indoor to outdoor agriculture. *Sustainability* **15**, 11601. <https://doi.org/10.3390/su151511601> (2023).
13. Farid, A. B. et al. Software defect prediction using hybrid model (CBIL) of convolutional neural network (CNN) and bidirectional long short-term memory (Bi-LSTM). *PeerJ Comput. Sci.* **7**, e739 (2021).
14. Abdulraheem, M. I. et al. Soil hardness measurement using fiber Bragg grating sensor: Combined compression forces methodology. *Physica status solidi (RRL) Rapid Res. Lett.* **19**(5), 2400431 (2025).
15. Abdulraheem, M. I. et al. Recent applications of fiber Bragg grating sensors in humidity and water content detection in agriculture: A comprehensive review of development, challenges, and future trends. *Int. J. Precis. Eng. Manuf.* **25**(7), 1499–1524 (2024).
16. Mor, S. et al. Current opportunities and trends in the gas sensor market: A focus on e-noses and their applications in food industry. *Chemosensors* **13**, 181. <https://doi.org/10.3390/chemosensors13050181> (2025).
17. Jin, J. et al. A complex-valued variant-parameter robust zeroing neural network model and its applications. *IEEE Trans. Emerg. Top. Comput. Intell.* **8**(2), 1303–1321 (2024).
18. Acharyya, S. & Kumar Guha, P. Enhanced formaldehyde sensing performance employing plasma-treated hierarchical  $\text{SnO}_2$  nanosheets through oxygen vacancy modulation. *Appl. Surf. Sci.* **655**, 159640 (2024).
19. Acharyya, S. & Guha, P. K. Hierarchical zinc Stannate nanoneedle-based sensitive detection of formaldehyde. *ACS Appl. Electron. Mater.* **5**(6), 3446–3453 (2023).
20. Samui, R. et al. SnSe nanoflakes for a  $\text{NO}_2$  sensor at room temperature. *ACS Appl. Nano Mater.* **7**(20), 24281–24290 (2024).
21. Mahata, B. et al. Temperature tunable selective detection of toluene and isopropanol employing plate-like  $\text{WO}_3$ -based single chemiresistor. *IEEE Sens. J.* **24**(21), 33970–33977 (2024).
22. Lou, C. et al. Design and optimization strategies of metal oxide semiconductor nanostructures for advanced formaldehyde sensors. *Coord. Chem. Rev.* **452**, 214280 (2022).
23. Xie, J. et al. Solid-state synthesis of Y-doped  $\text{ZnO}$  nanoparticles with selective-detection gas-sensing performance. *Ceram. Int.* **42**(1, Part A), 90–96 (2016).
24. Abdulraheem, M. I. et al. Advancement of remote sensing for soil measurements and applications: A comprehensive review. *Sustainability* **15**, 15444. <https://doi.org/10.3390/su152115444> (2023).

25. Ahmed, S. & Sinha, S. K. Studies on nanomaterial-based p-type semiconductor gas sensors. *Environ. Sci. Pollut. Res.* **30**(10), 24975–24986 (2023).
26. Stinn, J. P. et al. Ammonia and greenhouse gas emissions from a modern U.S. swine breeding-gestation-farrowing system. *Atmos. Environ.* **98**, 620–628 (2014).
27. Zhuang, M. et al. Different characteristics of greenhouse gases and ammonia emissions from conventional stored dairy cattle and swine manure in China. *Sci. Total Environ.* **722**, 137693 (2020).
28. Joo, H.-S. et al. Greenhouse gas emissions from naturally ventilated freestall dairy barns. *Atmos. Environ.* **102**, 384–392 (2015).
29. Zahmatkesh, I., Emdad, H. & Alishahi, M. M. Navier–Stokes computation of some gas mixture problems in the slip flow regime. *Sci. Iran.* **22**(1), 100338 (2015).
30. Fauzi, F. et al. Gas and humidity sensing with quartz crystal microbalance (QCM) coated with graphene-based materials—A mini review. *Sens. Actuators A* **330**, 112837 (2021).
31. Li, J. et al. Flexible pressure, humidity, and temperature sensors for human health monitoring. *Adv. Healthcare Mater.* **13**(31), 2401532 (2024).
32. Liu, Y. et al. Differences in responses of ammonia volatilization and greenhouse gas emissions to straw return and paddy-upland rotations. *Environ. Sci. Pollut. Res.* **29**(17), 25296–25307 (2022).
33. Ngwabie, N. M. et al. Effects of animal activity and air temperature on methane and ammonia emissions from a naturally ventilated building for dairy cows. *Atmos. Environ.* **45**(37), 6760–6768 (2011).
34. Joo, H. S. et al. Particulate matter dynamics in naturally ventilated freestall dairy barns. *Atmos. Environ.* **69**, 182–190 (2013).
35. Ni, J. Q. & Heber, A. J. Sampling and measurement of ammonia concentration at animal facilities—A review (2001).
36. Miao, H. et al. DFT analysis of the sensitivity of graphene/MoS<sub>2</sub> heterostructures toward H<sub>2</sub>CO. *Vacuum* **214**, 112182 (2023).
37. Chen, X. et al. Antiferroelectric SnO<sub>2</sub> network with amorphous surface for electrochemical N<sub>2</sub> fixation. *Angewandte Chemie Int. Ed.* **e202515222** (2025)
38. Peng, H. & Perdew, J. P. Rehabilitation of the Perdew–Burke–Ernzerhof generalized gradient approximation for layered materials. *Phys. Rev. B* **95**(8), 081105 (2017).
39. Moellmann, J. & Grimme, S. DFT-D3 study of some molecular crystals. *J. Phys. Chem. C* **118**(14), 7615–7621 (2014).
40. Lehtomäki, J. et al. Orbital-free density functional theory implementation with the projector augmented-wave method. *J. Chem. Phys.* **141**(23), 234102 (2014).
41. Warmbier, R. & Quandt, A. Brillouin zone grid refinement for highly resolved ab initio THz optical properties of graphene. *Comput. Phys. Commun.* **228**, 96–99 (2018).
42. Qiao, Y. et al. A multihead attention self-supervised representation model for industrial sensors anomaly detection. *IEEE Trans. Industr. Inf.* **20**(2), 2190–2199 (2024).
43. Zhao, H. et al. High-sensitivity and self-powered flexible pressure sensor based on multi-scale structured piezoelectric composite. *Chem. Eng. J.* **519**, 164787 (2025).
44. Qin, X. et al. Theoretical study of gas sensing toward acetone by a single-atom transition metal (Sc, Ti, V, and Cr)-doped InP<sub>3</sub> monolayer. *ACS Omega* **9**(45), 45059–45067 (2024).
45. Meng, X., et al., Identification of thermal fault states in cable insulation sheaths based on gas sensor arrays. *IEEE Trans. Dielectrics Electr. Insul.* 1–1 (2025).
46. Abdulraheem, M. I. et al. Recent advances in dielectric properties-based soil water content measurements. *Remote Sens.* **16**, 1328. <https://doi.org/10.3390/rs16081328> (2024).

## Author contributions

Mengying Du: Conceptualization, Visualization, Validation, Data acquisition, Writing—original draft, Writing—review & editing. Mukhtar Iderawumi Abdulraheem: Conceptualization, Visualization, Validation, Data acquisition, Writing—original draft, Writing—review & editing. Lulu Xu: Conceptualization, Resources, Writing—review & editing. Yiheng Zang: Data acquisition, Writing—review & editing. Yinghang Song: Validation, Writing—review & editing. Maryam Abbasi Tarighat: Validation, Writing—review & editing, data analyzing, Supervision. Vijaya Raghavan: Writing—review & editing, Supervision. Jiandong Hu: Conceptualization, Visualization, Writing—review & editing, Supervision, Funding acquisition.

## Funding

This work was supported by the 14th Five-Year National Key Research and Development Program (2021YFD1700904) and by the Major Science and Technology projects of Henan Province (221111320700). It was also supported by the Henan Center for Outstanding Overseas Scientists (GZS2021007).

## Declarations

### Competing interests

The authors declare no competing interests.

### Additional information

Correspondence and requests for materials should be addressed to M.I.A., M.A.T. or J.H.

Reprints and permissions information is available at [www.nature.com/reprints](http://www.nature.com/reprints).

**Publisher's note** Springer Nature remains neutral with regard to jurisdictional claims in published maps and institutional affiliations.

**Open Access** This article is licensed under a Creative Commons Attribution-NonCommercial-NoDerivatives 4.0 International License, which permits any non-commercial use, sharing, distribution and reproduction in any medium or format, as long as you give appropriate credit to the original author(s) and the source, provide a link to the Creative Commons licence, and indicate if you modified the licensed material. You do not have permission under this licence to share adapted material derived from this article or parts of it. The images or other third party material in this article are included in the article's Creative Commons licence, unless indicated otherwise in a credit line to the material. If material is not included in the article's Creative Commons licence and your intended use is not permitted by statutory regulation or exceeds the permitted use, you will need to obtain permission directly from the copyright holder. To view a copy of this licence, visit <http://creativecommons.org/licenses/by-nc-nd/4.0/>.

© The Author(s) 2025